CONTRACT NAS5-21798, "STUDIES OF SOUNDINGS AND IMAGING MEASUREMENTS FROM GEOSTATIONARY SATELLITES"

Verner E. Suomi, Director
The University of Wisconsin
Space Science and Engineering Center
1225 West Dayton Street
Madison, Wisconsin 53706

February 1973
Quarterly Report for Period 1 November 1972 - 31 January 1973

Prepared for

NATIONAL AERONAUTICS AND SPACE ADMINISTRATION
GODDARD SPACE FLIGHT CENTER

Greenbelt, Maryland 20771

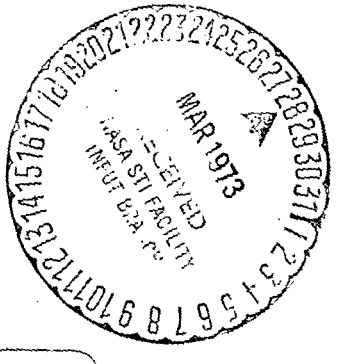

TECHNICAL REPORT STANDARD TITLE PAGE

1. Report No.	2. Government Accession No.	3. Recipient's Catalog No.

4. Title and Subtitle	5. Report Date
STUDIES OF SOUNDINGS AND IMAGING MEASUREMENTS FROM GEOSTATIONARY SATELLITES	February 1973
	6. Performing Organization Code
7. Author(s) Verner E. Suomi	8. Performing Organization Report No.
9. Performing Organization Name and Address The University of Wisconsin Space Science and Engineering Center 1225 West Dayton Street Madison, WI 53706	10. Work Unit No.
	11. Contract or Grant No.
	13. Type of Report and Period Covered Quarterly Report 1 November 1972 - 31 January 1973
12. Sponsoring Agency Name and Address GODDARD SPACE FLIGHT CENTER Greenbelt, Maryland 20771	14. Sponsoring Agency Code

15. Supplementary Notes

16. Abstract

This is the second Quarterly Report on "Studies of Soundings and Imaging Measurements from Geostationary Satellites." The report covers work performed during the quarter on four related studies.

17. Key Words (Selected by Author(s))	18. Distribution Statement
Meteorology Sun Glitter Cloud Growth Rate Satellite Stability	

19. Security Classif. (of this report)	20. Security Classif. (of this page)	21. No. of Pages	22. Price*
Unclassified	Unclassified	13	

*For sale by the Clearinghouse for Federal Scientific and Technical Information, Springfield, Virginia 22151.

Figure 2. Technical Report Standard Title Page

TABLE OF CONTENTS

Preface

This is the second quarterly report on Contract NAS5-21798, "Studies of Soundings and Imaging Measurements from Geostationary Satellites." During the past three months, good progress has been made on all tasks. The prototype Man-computer Interactive Data Access (McIDAS) equipment has operated well following repair of both the tape drives and the video disk recorder.

Introduction

This second quarterly report covers work performed from 1 November 1972 through 31 January 1973. In summary, progress by task is as follows:

Task A. Investigations of Meteorological Data Processing Techniques

Significant progress has been made in analysing and differentiating the several forms of line start errors in ATS image data. An earth edge detection algorithm has been thoroughly tested and is producing good data for error analysis. Comparisons of earth edge errors and landmark displacements show very close correlation, which confirms line start jitter as a major error source in wind computation. Initial tests indicate line start errors probably must be removed before correlation lag computations are made, but the reasons for these findings are not fully understood at this time. Work during the next quarter will concentrate on development of error removal techniques. Work on bispectral cloud height determination has been temporarily suspended pending acquisition of data suitable for testing concepts reported earlier.

Task B. Sun Glitter

Work on this task has been limited to description of the geometry involved because the graduate student working on this task has shifted her efforts to a different task in response to guidance from her advisory committee. Work should recommence during the next quarter.

Task D. Cloud Growth Rate

The early analyses in which correlations were sought relating cloud thickness to cloud brightness as seen in ATS images produced experimental results significantly different from theoretical results reported by other investigators. Work during this quarter has concentrated on exploring the hypothesis that the departure of observed data from theoretical predictions may be caused by differences in backscatter characteristics of ice particles and water droplets. Results from this investigation should be available during the next quarter.

Task E. Comparative Studies in Satellite Stability

Parts IV and V of the mathematical description of the stability model being developed by Mr. Das were attached to the last two monthly progress reports. Included in this report are the appendices to Mr. Das' report for those who now hold a set of the five parts previously submitted. The entire report, as well as additional information, will appear in the final report for this contract. Good progress has been made in coding the stability model for the 1108 computer and should be nearly completed by the end of the next quarter.

During this quarter the serious mechanical problems which had limited our use of the McIDAS equipment were corrected and the system is now working well. The problem of earth edge, or "line start," jitter in the ATS data is now the most serious problem affecting our ability to produce highly accurate

quantitative information from ATS data. We are confident this problem is tractable and our major effort is devoted to its solution.

On 1 February we were requested by competent NASA authority to restructure our efforts under this contract to accommodate a new task and we have agreed to do so. The objective of the new task will be to explore and to develop in concept meteorological applications of a two-meter aperture optic earth observation system in earth synchronous orbit. This task relates very closely to Task F, which was deleted by NASA from our original proposal, and we welcome the opportunity to pursue this study.

Task Progress

Task A. Investigations of Meteorological Data Processing Techniques

1. The Problem:

Precision display hard copy ATS images frequently show obvious line start timing errors which appear as irregular deviations of the earth edge from a smooth curve. The characteristics of this jitter are quite variable. Line to line jitter of four to six elements (quite prevalent), sudden shifts of 10 to 15 elements, and slow meandering oscillations of up to 20 elements peak to peak have been observed. In some cases, all three forms are present simultaneously and present serious difficulties to wind computations based on frame to frame cloud motions, since the observed East-West motion is strongly affected by line start deviations.

To screen data for problems in line start timing and to understand and correct for its effects, an earth edge detection algorithm was developed and tested. The algorithm appears to be quite effective in detecting the earth edge consistently. However, successful utilization of the earth edge

information in correcting wind computation has not yet been achieved. Results to date and plans for future effort on this problem are discussed in the following.

2. Earth Edge Detection Algorithm:

The basic algorithm used in the earth edge detection program is a threshold detector with noise compensation. Starting at element N (a substantial distance to the left of the left earth edge) the average noise for the space view is obtained by averaging samples N to N + 50. The algorithm next looks along the scan line 14 elements ahead (to N + 64). If the samples from N + 64 to N + 68 all exceed the sum of the mean space noise and a pre-set threshold value, then N + 64 is returned as the position of the earth edge. If the condition is not met, N is increased by one element and the whole process is repeated. The 14 element buffer between space noise averaging and threshold testing is required to prevent averaging of signal with noise. The requirement that five successive samples exceed the offset threshold is needed to prevent triggering on isolated noise spikes. The use of a threshold offset by the mean space noise prevents line to line (or frame to frame) variations in noise from causing corresponding variations in the position of the detected earth edge.

The first tests with the algorithm were made with data from day 204, 1969, which showed considerable variations in noise amplitude and line start position as well. In addition to testing the algorithm's sensitivity to noise, a search was made for the optimum threshold. The optimum threshold should cause the algorithm to trigger at an altitude of 20 km to 30 km above the surface. At significantly lower altitudes variations in cloud cover near the limb would cause erroneous variations in the position of the detected earth edge. A very

low threshold would cause triggering at a high altitude well above the clouds, but would also be very susceptible to noise in the signal.

Thresholds of 5, 10, 20, and 40 digital counts were tested (the ATS signal data ranges from 0 to 255 digital counts, the maximum signal roughly corresponding to the radiance of the brightest cloud). The 5 threshold displayed a significant correlation with noise variations and a large scatter as well. The 10 and 20 thresholds produced edges that were not noise correlated. The 40 threshold was not noise correlated, but did show large variations in edge position which were inconsistent with both expected jitter behavior and with the results of 10 and 20 thresholds. The 40 threshold thus appears to cause triggering on clouds. As a result of this preliminary testing, the 10 and 20 thresholds were chosen for standard usage.

In normal operation, the detection program finds edges for both 10 and 20 thresholds. The mean of these two is used for the final detected earth edge and the difference is used to check the quality of the detection. The difference is typically about three samples $\pm$ 2 RMS.

3. Comparison of Edge Detection and Landmark Measurements:

Landmark measurements made for navigation of ATS-3 images for day 204, 1969 are uniquely suited for testing the consistency of the earth edge detection algorithm. The landmark used was a small island off the coast of South America, which occupied approximately one ATS field of view and which could be isolated to one line and within one or two samples (most landmark measurements are based on patterns extending over many lines and elements). Neglecting earth rotation within the ATS data frame (this is justifiable for the case in question because the spin axis inclination is small), the landmark element position and the earth edge element position, for the same line on which the landmark falls, should differ by a constant. For a five frame sequence, this was found to be true

to within about 1.3 elements RMS. This sequence of comparisons revealed that the anomolous landmark motion previously discovered was indeed a result of line start timing errors.

4. Frame to Frame Comparison of Earth Edges:

Comparison of detected earth edge position as a function of line number with a smooth earth edge calculated by the SSEC ATS navigation program reveal moderate amplitude (4-8 elements) line to line jitter, sudden large shifts (10-15 elements) taking place within a few lines and lasting for many lines; and, perhaps most disturbing, large amplitude (up to 20 elements peak-to-peak) meandering oscillations with a varying period of the order of several hundred lines. The last effect is not readily observable in hard copy images, but is extremely important in the computation of frame to frame cloud motions.

Since the earth edge irregularities (and the inferred line start irregularities) are not the same in each frame, part of the observed cloud motion in the data frame is due to differences in line start timing errors. For many of the day 204, 1969 images, this motion is so large as to be readily observable on the SSEC McIDAS prototype TV display system when a sequence of images is viewed as a movie loop. The general characteristics of this motion were found to be in agreement with that predicted from the earth edge behavior, i.e., the latitude regions and sign of the erroneous motions appeared to be consistent with the relative motion of the detected earth edge. Certain regions of latitude which had the same line start timing error should appear as nulls in the anomolous motion. The position of these nulls also appeared to agree with predictions. All these approximate visual checks indicated that an accurate numerical check with analysis of digital data was warranted.

5. Correction of WINDCO Lags:

The WINDCO (wind computation) program uses either cross-correlation or Euclidean norm methods to measure the relative line and element motion (or lag) of a cloud mass from one frame to another. Assuming constant cloud velocity and perfect line start timing, the element lag between the first two frames of a three frame sequence (equally spaced in time) should be equal (approximately) to the element lag between the second two frames. When line start errors are present, the two lag results will be in disagreement. If the earth edge detection is consistent and the correlations are high, the disagreement in the two lags should be predictable from relative differences in earth edge position from frame to frame.

To test this hypothesis, approximately 20 cloud tracers were selected and lag computations processed. If the lag discrepancies agreed with the line start difference discrepancies, the feasibility of correcting lag computations for line start timing errors would be demonstrated. Results to date have, in fact, not demonstrated this. The results appear to indicate that the opposite is true, although a number of error sources have not been fully investigated at this time, among which are choice of poor cloud tracers, false correlations, and cloud size effects. It may turn out that the line start errors have to be corrected in the data before the lag computations are made instead of correcting them in the lags afterwards.

Task B. Sun Glitter

The following develops the geometry of polar satellite sun glint observations. The object is to find the location of the sun glint with respect to the satellite reference frame.

Consider an earth centered reference frame; $\hat{z}$ toward the north pole and $\hat{x}$ and $\hat{y}$ in the equatorial plane.

Define;	point S	location of sun
	point A	location of satellite
	point P	location of reflection
	R	radius of earth
	R + h	distance from center of earth to A
	point 0	center of earth
	ω	angle of incidence = angle of reflection
	I	angle between earths equatorial plane and the plane of the orbit

It is assumed that the positions of the sun and the satellite are known at all times, i.e., $\overline{S}(\theta_S(\tau), \phi_S(\tau)$ and $\overline{A}(\theta_A(\tau), \phi_A(\tau))$ are known. It was necessary to find $\overline{P} = \overline{P}[\theta_S(\tau)\phi_S(\tau)\theta_A(\tau)\phi_A(\tau)]$.

If there were no wind the ocean would be smooth and the vector $\overline{P}$ would be in the plane described by $\overline{S}$ and $\overline{A}$. Therefore, a relation between ϕ_p and Θ_p is available. Furthermore, the normal to the surface at point P is

$$\overline{n} = \frac{\overline{S}}{|S|} + \frac{\overline{A}-\overline{P}}{|\overline{A}-\overline{P}|} \qquad \text{where } |n| = (2-2\cos 2\omega)^{1/2}.$$

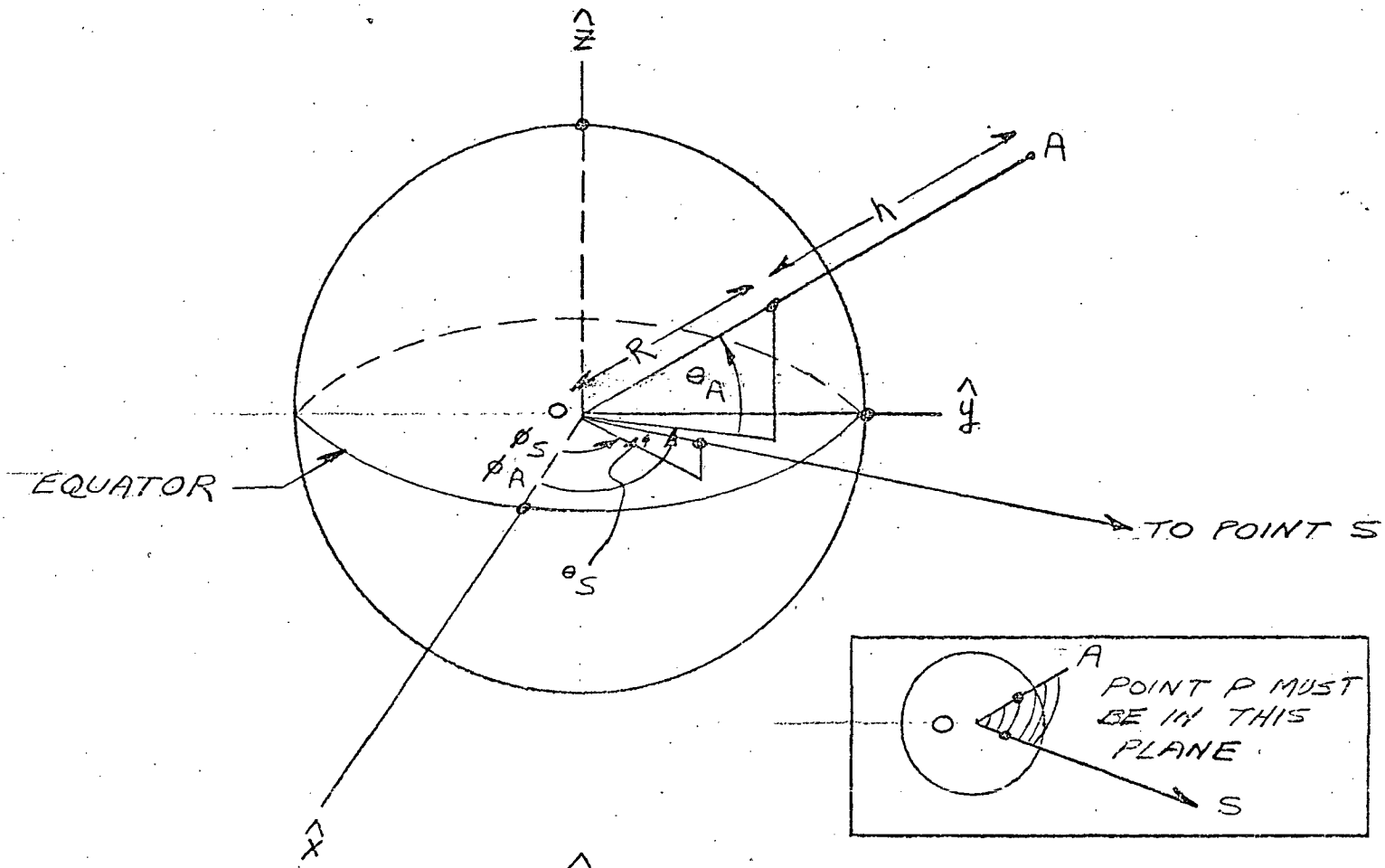
Ẑ
A
h
R
θA
O
ŷ
φS
φA
EQUATOR
TO POINT S
θS
X̂
A
POINT P MUST BE IN THIS PLANE
O
S

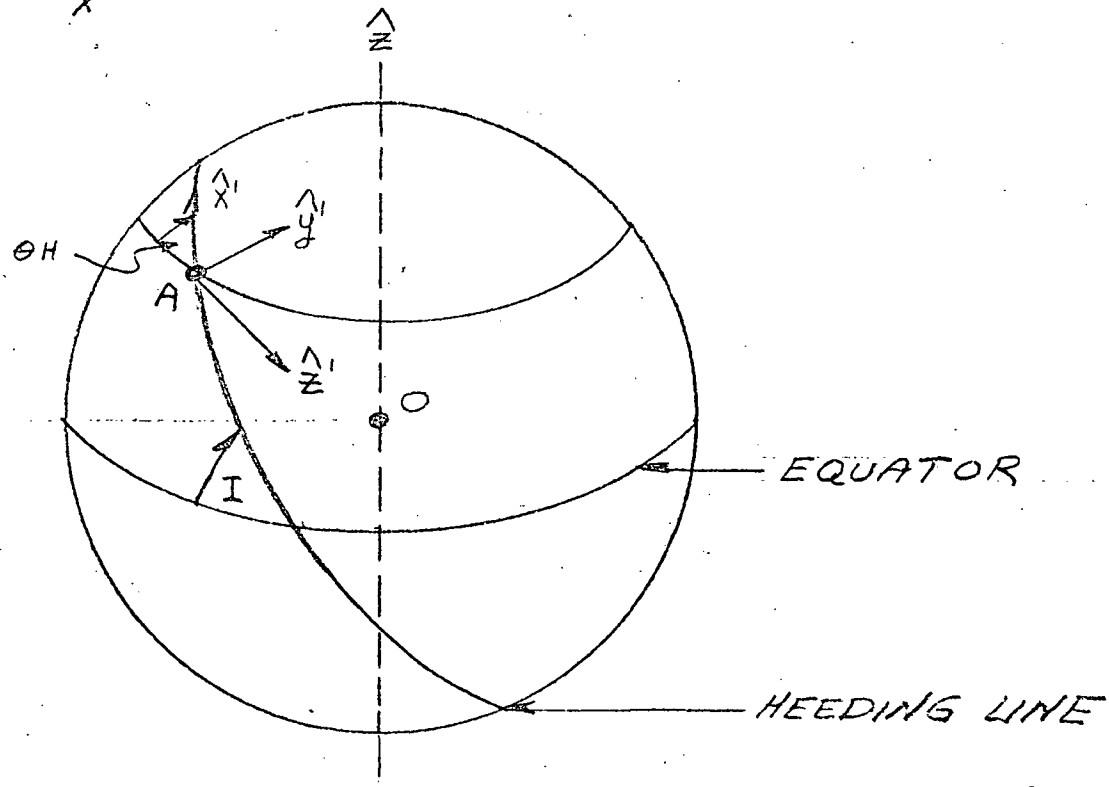
Ẑ
X̂'
ŷ'
θH
A
Ẑ'
O
I
EQUATOR
HEEDING LINE

Third, $$\frac{\bar{n}}{|n|} - \frac{\bar{A}-\bar{P}}{|A-P|} = \cos\omega = \frac{\bar{n}}{|n|} \cdot \frac{\bar{S}}{|S|}$$

so there are three quations and three unknowns, Θ_p, ϕ_p, ω. With this information, it is clear that the vector $\bar{P}$ can be found such that

$$\bar{P} = R\frac{\bar{n}}{|n|} = \bar{P}(\Theta_A, \phi_A, \Theta_S, \phi_S)$$

Now consider the satellite reference frame such that

$\hat{x}'$ along heading line

$\hat{y}'$ $\perp$ heading line

$\hat{z}'$ toward the center of the earth

Let the rotation matrix which rotates the earth centered reference frame into the satellite reference frame be represented by $\theta(t)$. Let $\bar{a}$ be any vector in the earth system and $\bar{a}'$ be the vector in the satellite system. Then $\bar{a} = \theta(t)[\bar{a}-\bar{A}] = \theta(t)\bar{a} - (R+h)\hat{z}'$. With this matrix $\bar{P}'$, the position of the sun glint in the satellite coordinate system, can be calculated at all times.

For easiest analysis of the sea slope the camera should be pointed directly along $\bar{P}$. For this orientation the relationship between the photo coordinates and the isolines of constant slope is the simplest.

$$\Theta(t) = \begin{pmatrix} \cos\theta_H\sin\theta_A+\sin\theta_H\sin\theta_A\cos\theta_A & -\cos\theta_H\cos\theta_A+\sin\theta_H\sin\theta_A\sin\theta_A & -\sin\theta_H\cos\theta_A \\ -\sin\theta_A\sin\theta_H+\cos\theta_H\sin\theta_A\cos\theta_A & \sin\theta_H\cos\theta_A+\cos\theta_H\sin\theta_A\sin\theta_A & -\cos\theta_H\cos\theta_A \\ \cos\theta_A\cos\theta_A & \cos\theta_A\sin\theta_A & \sin\theta_A \end{pmatrix}$$

where $\cos\theta_H = \frac{\cos I}{\cos\theta_A}$ and $\tan\theta_H = \frac{\sqrt{\sin^2 I - \sin^2\theta_A}}{\cos I}$

Θ_H is the angle between the heading line and the plane parallel to the equatorial surface.

B

Task D. Cloud Growth Rate Study

To parameterize convection, one of the basic quantities which must be measured is the volume flux through a cloud. Previous work on evaluating convective heat transport from a geosynchronous satellite, such as done by Sikdar (1971), determined the volume flux by measuring the horizontal divergence of the cirrus outflow of convective towers. However, the thickness of cirrus anvil was not known so an assumed value was used. To improve the estimates of volume flux, the thickness of the cirrus outflow must be determined for each cloud measured.

A satellite sees a strong brightness gradient on convective clouds. One parameter which determines the brightness of a cloud is its thickness. The theoretical work of E. Hewson as presented in Kondratyev's "Actinometry" shows the dependence of the cloud's reflectivity on cloud brightness. However, the reflectivity reaches 80% for clouds several hundred meters thick and remains virtually constant for cloud thickness over 600 m. Hence, thick clouds should be uniformly bright, but satellite's do not see this happening. The difference could lie in the fact that almost all theoretical work on scattering has been done using the sphere as the geometry of the scattering particle. At present no measurements of the volume phase matrix for ice crystal clouds has been made available ("Major Problems in Atmospheric Radition" - Atmospheric Radiation Working Group, Bulletin of the AMS October, 1972). If it were, present methods could provide solutions to radiative transfer problems. Experimental work, such as by Huffman and Thursby (JAS, 1969) has shown that ice crystals have different scattering properties than spheres. A theoretical study by Liou (JAS, 1972) using long horizontal randomly oriented cylinders has shown that cylinders have considerable less back scatter than polydispersed spheres.

Since a satellite is looking at the top of a cloud, the scattering particles which the satellite sees are mainly ice crystals for a deep cloud. If ice crystals and rain drops have different scattering properties, then the brightness gradient could be caused by the different amounts of the two water forms in a cloud. If this were so, then the angular scattering dependence of the bright parts of the cloud should be different from that of the rest of the cloud. Analysis of this problem is presently being worked upon. Analysis routines have been written and a test set of convecting clouds in the Caribbean has been selected. The McIDAS system has been used to obtain access to the data. Analysis is presently being performed on the data, but no results have been obtained yet.

Task E. Comparative Studies in Satellite Stability

The mathematical development of the stability model has been completed and the model is now being coded for the 1108 computer. The appendices to the previously submitted mathematical analysis report are attached to this progress report.

New Technology

No items of new technology have been produced during this quarter.

Program for Next Reporting Interval

Task A. Investigations of Meteorological Data Processing Technique

Continued work on the problem of ATS line start jitter is directed at the following tasks:

1) Theoretical calculations of atmospheric limb radiance profiles, including investigations of the effects of sun angle, latitude, ozone, aerosols and atmospheric state;

2) Improvement of the edge detection algorithm to take account of the results of task (1) and to be more efficient in terms of cost and time;
3) Application of the algorithm to study line start error characteristics for a wider selection of ATS data;
4) Futher effort to correlate east-west residuals in wind computations with line start errors inferred from earth edge detection;
5) Development of an algorithm to detect the position of the right hand earth edge; and
6) Implementation of earth edge detection in routine data processing.

Task B. Sun Glitter

Work on this task depends upon availability of qualified graduate student assistance. This task will be curtailed to provide funds for the new Task H.

Task D. Cloud Growth Rate

Attempts will be made to differentiate and measure relative backscatter characteristics of liquid and ice cloud forms using McIDAS.

Task E. Comparative Studies in Satellite Stability

The next quarter will be devoted entirely to coding and debugging the stability model in the 1108 computer.

Task H. Large Optics Applications Study

A broadly based study effort will be organized and pursued within SSEC, in a graduate seminar, and in conversations with persons in NASA and other government agencies.

Conclusions and Recommendations

None at this time.

APPENDIX 1

The Form of G_B and $\underline{q}_B^*$

The (110 x 1) generalized position vector q_{Bi}^*, i = 1 - 110, consists of the time-dependent coefficients introduced with the assumed displacement functions of the structural elements of the body B. The coefficients for each element of $\underline{q}_B^*$ are listed below.

Element No.	Element Name	Element No.	Element Name
1	$y_{17,1}$	19	$^3q_{1,3}$
2	$y_{17,2}$	20	$q_{2,1}$
3	$y_{17,3}$	21	$^1q_{2,2}$
4	$y_{18,1}$	22	$^2q_{2,2}$
5	$y_{18,2}$	23	$^3q_{2,2}$
6	$y_{18,3}$	24	$^1q_{2,3}$
7	$y_{19,1}$	25	$^2q_{2,3}$
8	$y_{19,2}$	26	$^3q_{2,3}$
9	$y_{19,3}$	27	$q_{3,1}$
10	$y_{20,1}$	28	$^1q_{3,2}$
11	$y_{20,2}$	29	$^2q_{3,2}$
12	$y_{20,3}$	30	$^3q_{3,2}$
13	$q_{1,1}$	31	$^1q_{3,3}$
14	$^1q_{1,2}$	32	$^2q_{3,3}$
15	$^2q_{1,2}$	33	$^3q_{3,3}$
16	$^3q_{1,2}$	34	$q_{4,1}$
17	$^1q_{1,3}$	35	$^1q_{4,2}$
18	$^2q_{1,3}$	36	$^2q_{4,2}$

Element No.	Element Name	Element No.	Element Name
37	${}^{3}q_{4,2}$	63	$\chi_{2,7}$
38	${}^{1}q_{4,3}$	64	$\chi_{2,8}$
39	${}^{2}q_{4,3}$	65	$\chi_{2,9}$
40	${}^{3}q_{4,3}$	66	$\chi_{2,10}$
41	y_{13}	67	$\chi_{2,11}$
42	y_{14}	68	$\chi_{2,12}$
43	y_{15}	69	$\chi_{2,13}$
44	y_{16}	70	$\chi_{2,14}$
45	y_{1}	71	$\chi_{2,15}$
46	$\psi_{1,1}$	72	$\chi_{2,16}$
47	$\psi_{1,2}$	73	$\chi_{2,17}$
48	y_{2}	74	$\chi_{2,18}$
49	$\psi_{2,1}$	75	$a_{2,13}$
50	$\psi_{2,2}$	76	$a_{2,14}$
51	$a_{2,1}$	77	$a_{2,15}$
52	$a_{2,2}$	78	$\chi_{2,1}$
53	$a_{2,3}$	79	$a_{1,1}$
54	$a_{2,4}$	80	$a_{1,2}$
55	$a_{2,5}$	81	$a_{1,3}$
56	$a_{2,6}$	82	$a_{1,4}$
57	$a_{2,7}$	83	$a_{1,5}$
58	$a_{2,8}$	84	$a_{1,6}$
59	$a_{2,9}$	85	$a_{1,7}$
60	$a_{2,10}$	86	$a_{1,8}$
61	$a_{2,11}$	87	$a_{1,9}$
62	$a_{2,12}$	88	$a_{1,10}$

89	$a_{1,11}$	100	b_{11}
90	$a_{1,12}$	101	b_{10}
91	$\chi_{1,8}$	102	b_9
92	$\chi_{1,9}$	103	b_8
93	$\chi_{1,10}$	104	b_7
94	$\chi_{1,11}$	105	b_6
95	$a_{1,13}$	106	b_5
96	$a_{1,14}$	107	b_4
97	$a_{1,15}$	108	b_3
98	$\chi_{1,7}$	109	b_2
99	$\chi_{1,1}$	110	b_1

The constant matrix $[G_B]$ is defined by

$$\underline{C}_B = [G_B]\underline{q}_B^*$$

In this equation, $\underline{C}_B$ is a (3 x 1) vector and is the shift of the center of mass of the satellite. Hence $[G_B]$ is a (3 x 110) matrix. The nonzero elements of $[G_B]$ are listed below. All elements are to be divided by $-\|M\|_B$.

FIRST ROW

Column No.	Element	Column No.	Element
1	m_{17}	4	m_{18}
7	m_{19}	10	m_{20}
13	$b^{\rho_1 \cdot \ell}$	21	$\frac{1}{p_1} b^{\rho_2}(e^{p_1 \ell} - 1) - b^{\rho_2 \cdot \ell}$
22	$\frac{1}{2} b^{\rho_2 \cdot \ell^2}$	23	$b^{\rho_2 \cdot \ell}$
27	$- b^{\rho_3 \cdot \ell}$	35	$- \frac{1}{p_1} b^{\rho_4}(e^{p_1 \ell} - 1) + b^{\rho_4 \cdot \ell}$
36	$- \frac{1}{2} b^{\rho_4 \cdot \ell^2}$	37	$- b^{\rho_4 \cdot \ell}$
107	$2a_B \, s^{\rho_B \cdot \ell_s}$		

SECOND ROW

2	m_{17}	5	m_{18}
8	m_{19}	11	m_{20}
14	$\frac{1}{p_1} b^{\rho_1}(e^{p_1 \ell} - 1) - b^{\rho_1 \cdot \ell}$	15	$\frac{1}{2} b^{\rho_1 \cdot \ell^2}$
16	$b^{\rho_1 \cdot \ell}$	20	$- b^{\rho_2 \cdot \ell}$
28	$- \frac{1}{p_1} b^{\rho_3}(e^{p_1 \ell} - 1) + b^{\rho_3 \cdot \ell}$	29	$- \frac{1}{2} b^{\rho_3 \cdot \ell^2}$
30	$- b^{\rho_3 \cdot \ell}$	34	$b^{\rho_4 \cdot \ell}$
105	$2a_B \, s^{\rho_B \cdot \ell_s}$		

THIRD ROW

3	m_{17}	6	m_{18}
9	m_{19}	12	m_{20}
17	$\frac{1}{p_1} b^{\rho_1}(e^{p_1 \ell}-1) - b^{\rho_1}\cdot\ell$	18	$\frac{1}{2} b^{\rho_1}\cdot\ell^2$
19	$b^{\rho_1}\cdot\ell$	24	$\frac{1}{p_1} b^{\rho_2}(e^{p_1 \ell}-1) - b^{\rho_2}\cdot\ell$
25	$\frac{1}{2} b^{\rho_2}\cdot\ell^2$	26	$b^{\rho_2}\cdot\ell$
31	$\frac{1}{p_1} b^{\rho_3}(e^{p_1 \ell}-1) - b^{\rho_3}\cdot\ell$	32	$\frac{1}{2} b^{\rho_3}\cdot\ell^2$
33	$b^{\rho_3}\cdot\ell$	38	$\frac{1}{p_1} b^{\rho_4}(e^{p_1 \ell}-1) - b^{\rho_4}\cdot\ell$
39	$\frac{1}{2} b^{\rho_4}\cdot\ell^2$	40	$b^{\rho_4}\cdot\ell$
41	m_{13}	42	m_{14}
43	m_{15}	44	m_{16}
45	m_1	48	m_2
63	$\alpha_1 p^{\rho_2} a_B^2$	64	$\alpha_2 p^{\rho_2} a_B^2$
65	Equal to element 64	66	Equal to element 63
67	Equal to 64	68	Equal to 63
69	Equal to 63	70	Equal to 64
71	Equal to 64	72	Equal to 64
73	Equal to 64	74	Equal to 64
75	$\frac{p^{\rho_2}}{p^{\rho_1}}\cdot\alpha_3$	76	$-\frac{\pi}{10} a_B^2 p^{\rho_2}$
77	$-\frac{\pi}{15} a_B^2 p^{\rho_2}$	78	$\pi a_B^2 p^{\rho_2}$
91	$-\alpha_2 p^{\rho_1} a_B^2$	92	Equal to 91
93	Equal to 91	94	Equal to 91
95	$2\pi p^{\rho_1} a_B^2 \alpha_3$	96	$-\frac{\pi}{10} a_B^2 p^{\rho_1}$
97	$-\frac{\pi}{15} p^{\rho_1} a_B^2$	98	$-\frac{\pi}{8} p^{\rho_1} a_B^2$
99	$\pi p^{\rho_1} a_B^2$		

In the above,

$$\alpha_1 = \int_0^1 \int_0^{2\pi} [r^2 - 2\alpha' r \cos\theta + (\alpha')^2] \log \left[\frac{r^2 - 2\alpha' r \cos\theta + (\alpha')^2}{1 - 2\alpha' r \cos\theta + (\alpha')^2 r^2} \right] r d\theta dr$$

$$\alpha_2 = \int_0^1 \int_0^{2\pi} (r^2 - 2\alpha r \cos\theta + \alpha^2) \log \left(\frac{r^2 - 2\alpha r \cos\theta + \alpha^2}{1 - 2\alpha r \cos\theta + \alpha^2 r^2} \right) r d\theta dr \ .$$

$$\alpha_3 = \frac{1}{\lambda_0^2} \int_0^{\lambda_0} J_0(x) x dx; \quad J_0(\lambda_0) = 0$$

$$= 0.215922106463.$$

The distance of the singular points from the center of the plate are denoted by α and α'.

APPENDIX 3

Reduced Equations for Beams

Let the (3 x 7) functional matrix $[{}_bK_i]$ be defined by

$$\{{}_bq_i\} = [{}_bk_i]\{{}_bq_i^*\} \tag{A3.1}$$

Then the elements of $[{}_bk_i]$ are given by

$$[{}_bK_i] = \begin{bmatrix} 1 & 0 & 0 & 0 & 0 & 0 & 0 \\ 0 & (e^{p_1 s}-1) & s & 1 & 0 & 0 & 0 \\ 0 & 0 & 0 & 0 & (e^{p_1 s}-1) & s & 1 \end{bmatrix} \tag{A3.2}$$

We also have

$$(\mathcal{I} - \mathcal{I}_1) = \begin{bmatrix} 0 & 0 & 0 \\ 0 & 1 & 0 \\ 0 & 0 & 1 \end{bmatrix} \tag{A3.3}$$

Then from (Eqs. (1.22) and (1.23), we get

$$[{}_bA_{i1}] = \begin{bmatrix} (\mathcal{I} - \mathcal{I}_1)\int_0^{\ell} [{}_bK_i]ds \\ (\mathcal{I} - \mathcal{I}_1)\int_0^{\ell} [{}_bK_i]\, e^{p_1 s} ds \\ \int_0^{\ell} [{}_bK_i]sds \end{bmatrix} {}_b\rho_i \tag{A3.4}$$

We now introduce the (3 x 7) matrices $[{}_bK_{i2}]$ and $[{}_bK_{i3}]$, of which the the nonzero elements are given by

$$[{}_bK_{i2}]_{2,2} = -({}_bE_i)({}_bI_{i,3})({}_b\tau_i)p_1^3\, e^{p_1 s}\, \kappa^*_{T_{i,2}} \sin\alpha_{i,2} \tag{A3.5}$$

$$[{}_bK_{i2}]_{3,5} = -({}_bE_i)({}_bI_{i,2})({}_b\tau_i)p_1^3\, e^{p_1 s}\, \kappa^*_{T_{i,3}} \sin\alpha_{i,3} \tag{A3.6}$$

$$[{}_bK_{i3}]_{2,2} = ({}_bE_i)({}_bI_{i,3})p_1^3\, e^{p_1 s}(p_1 + \kappa^*_{T_{i,2}} \sin\alpha_{i,2}) \tag{A3.7}$$

$$[{}_bK_{i3}]_{3,5} = ({}_bE_i)({}_bI_{i,2})p_1^3 e^{p_1 s}(p_1 + \kappa^*_{T_{i,3}} \sin \alpha_{i,3}) \qquad (A3.8)$$

Using Eqs. (A3.5) and (A3.6), the (7 x 7) matrix $[{}_bA_{i2}]$ is obtained as

$$[{}_bA_{i2}] = \begin{bmatrix} (\mathcal{I} - \mathcal{I}_1)\{2\ {}_b\rho_i\ \omega_B^* \int_0^\ell [{}_bK_i]ds - \int_0^\ell [{}_bK_{i2}]ds \\ (\mathcal{J} - \mathcal{J}_1)\{2\ {}_b\rho_i \omega_B^* \int_0^\ell [{}_bK_i]e^{p_1 s} ds - \int_0^\ell [{}_bK_{i2}]e^{p_1 s} ds\} \\ \{2\ {}_b\rho_i\ \omega_B^* \int_0^\ell [{}_bK_i]sds - \int_0^\ell [{}_bK_{i2}]sds\} \end{bmatrix} \qquad (A3.9)$$

From Eqs. (A3.7) and (A3.8), the (7 x 7) matrix $[{}_bA_{i3}]$ is obtained as

$$[{}_bA_{i3}] = \begin{bmatrix} (\mathcal{I} - \mathcal{I}_1)\{{}_b\rho_i(\dot{\omega}_B^* + \omega_B^{**}) \int_0^\ell [{}_bK_i]ds - \int_0^\ell [{}_bK_{i3}]ds\} \\ (\mathcal{J} - \mathcal{J}_1)\{{}_b\rho_i(\dot{\omega}_B^* + \omega_B^{**}) \int_0^\ell [{}_bK_i]e^{p_1 s} ds - \int_0^\ell [{}_bK_{i3}]e^{p_1 s} ds\} \\ \{{}_b\rho_i(\dot{\omega}_B^* + \omega_B^{**}) \int_0^\ell [{}_bK_i]sds - \int_0^\ell [{}_bK_{i3}]sds\} \end{bmatrix} \qquad (A3.10)$$

It is to be noted that, in the absence of external forces,

$$\ddot{\Theta X}_B = \frac{1}{\|M\|_B} \underline{F}_{BC} \qquad (A3.11)$$

Therefore from Eq. (1.103), we get

$$\ddot{\Theta X}_B = \frac{1}{\|M\|_B}\{(\frac{1}{\gamma}\tau_1 - \tau_2)G_B\underline{q}_B^* + (\frac{1}{\gamma}\tau_7 - \tau_8)G_B\underline{q}_B^*$$

$$- (\tau_3\underline{\theta} + \tau_9\dot{\underline{\theta}}) \qquad (A3.12)$$

Hence from Eqs. (1.22) and (1.23), the (7 x 1) vector $\{{}_bA_{i4}\}$ is obtained as

$$\{{}_bA_{i4}\} = \begin{bmatrix} (\mathscr{A}-\mathscr{A}_1)({}_b\rho_i)\{(\dot{\omega}_B^* + \omega_B^{**})\int_0^{\ell} \underline{R}_i ds - \frac{\ell}{\|M\|_B}[\mu_i^B](\tau_3\underline{\theta} + \tau_9\dot{\underline{\theta}})\} \\ (\mathscr{A}-\mathscr{A}_1)({}_b\rho_i)\{(\dot{\omega}_B^* + \omega_B^{**})\int_0^{\ell} \underline{R}_i\, e^{p_1 s} ds - \frac{(e^{p_1\ell}-1)}{p_i\|M\|_B}(\tau_3\underline{\theta} + \tau_9\dot{\underline{\theta}})\} \\ ({}_b\rho_i)\{(\dot{\omega}_B^* + \omega_B^{**})\int_0^{\ell} \underline{R}_i s ds - \frac{\ell^2}{2\|M\|_B}(\tau_3\underline{\theta} + \tau_9\dot{\underline{\theta}})\} \end{bmatrix}$$

(A3.13)

In the above equation

$$\underline{R}_i = \begin{Bmatrix} R_{i,1} + s \\ R_{i,2} \\ R_{i,3} \end{Bmatrix} \tag{A3.14}$$

The forms of the (7 x 3) matrices $[\lambda_1]$, $[\lambda_2]$ and $[\lambda_3]$ will now be obtained.

$$[\lambda_1] = \begin{bmatrix} ({}_b\rho_i)(\mathscr{A}-\mathscr{A}_1)\ell[\mu_i^B] \\ ({}_b\rho_i)(\mathscr{A}-\mathscr{A}_1)\frac{1}{p_1}(e^{p_1\ell}-1)[\mu_i^B] \\ ({}_b\rho_i)\frac{\ell^2}{2}[\mu_i^B] \end{bmatrix} \tag{A3.15}$$

$$[\lambda_2] = \begin{bmatrix} ({}_b\rho_i)(\mathscr{A}-\mathscr{A}_1)\ell[\mu_i^B]\{2\tilde{\omega}_B + \frac{1}{\|M\|_B}(\frac{1}{\gamma}\tau_7 - \tau_8)\} \\ ({}_b\rho_i)(\mathscr{A}-\mathscr{A}_1)\frac{1}{p_1}(e^{p_1\ell}-1)[\mu_i^B]\{2\tilde{\omega}_B + \frac{1}{\|M\|_B}(\frac{1}{\gamma}\tau_7 - \tau_8)\} \\ ({}_b\rho_i)\frac{\ell^2}{2}[\mu_i^B]\{2\tilde{\omega}_B + \frac{1}{\|M\|_B}(\frac{1}{\gamma}\tau_7 - \tau_8)\} \end{bmatrix}$$

(A3.16)

$$[\lambda_3] = \begin{bmatrix} ({}_b\rho_i)(\mathcal{J}-\mathcal{J}_1)\ell[\mu_i^B]\{(\dot{\tilde{\omega}}_B + \tilde{\omega}_B\tilde{\omega}_B) + \frac{1}{\|M\|_B}(\frac{1}{\gamma}\tau_1 - \tau_2)\} \\ ({}_b\rho_i)(\mathcal{J}-\mathcal{J}_1)\frac{1}{p_1}(e^{p_1\ell}-1)[\mu_i^B]\{(\dot{\tilde{\omega}}_B + \tilde{\omega}_B\tilde{\omega}_B) + \frac{1}{\|M\|_B}(\frac{1}{\gamma}\tau_1-\tau_2)\} \\ ({}_b\rho_i)(\mathcal{J}-\mathcal{J}_1)\frac{\ell^2}{2}[\mu_i^B]\{(\dot{\tilde{\omega}}_B + \tilde{\omega}_B\tilde{\omega}_B) + \frac{1}{\|M\|_B}(\frac{1}{\gamma}\tau_1 - \tau_2)\} \end{bmatrix}$$

(A3.17)

The value of p_1 is solved from Euler's beam solution with the following boundary conditions:

$$y(0) = \frac{dy}{ds}(0) = 0$$

$$[EI\frac{\partial^2 y}{\partial s^2} + mr^2\frac{\partial^3 y}{\partial s \partial t^2}]_{s=\ell} = 0$$

$$[EI\frac{\partial^3 y}{\partial s^3} + m\frac{\partial^2 y}{\partial t^2}]_{s=\ell} = 0$$

where m is the tip-mass and r is its radius of gyration about the junction point.

These conditions lead to the equation

$$\frac{1}{{}_b\rho_i}[({}_b\rho_i)^2 - m^2r^2p_1^4](1 - \cos p_1\ell \cosh p_1\ell) - mp_1(1 + r^2p_1^2)\cos p_1\ell \cosh p_1\ell$$

$$+ mp_1(1 - r^2p_1^2)\sin p_1\ell \cosh p_1\ell = 0 \qquad \text{(A3.18)}$$

APPENDIX 4

Remarks on the Plate Functions

Several forms of the plate function $\psi(z,w)$ have been shown on page 30, part I of this work. It will now be shown that the function $\psi_1^*(z,w)$ is the best choice. It is easily seen that the functions $\psi_i^*(z,w)$, $i = 3\text{-}6$, are included in ψ_1^* and ψ_2^*. Therefore, we now examine $\psi_2^*(z,w)$.

Let P be a lateral concentrated force applied by the plate on an attached system. Let v_x and v_y be the shear forces in the plate due to the deformation caused by the force P in the direction of the y- and x-axes, respectively. Then

$$P = -\oint_C [v_y dx + v_x dy] \tag{A4.1}$$

where C is a small circle of radius ε with its center at the point of application of the load P.

From Eq. (A4.1), we get

$$P = D \oint_C \{[\frac{\partial}{\partial y} \nabla^2\psi_2^*]dx + [\frac{\partial}{\partial x} \nabla^2\psi_2^*]dy\} \tag{A4.1a}$$

where ∇^2 is the Laplacian in x and y, and D is the stiffness of the plate, or

$$P = 4D \oint_C \left\{ \frac{\partial}{\partial y} [\frac{\partial^2\psi_2^*}{\partial z \partial \bar{z}}]dx + \frac{\partial}{\partial x}[\frac{\partial^2\psi_2^*}{\partial z \partial \bar{z}}]dy \right\}$$

$$= 4iD \oint_C \left\{ \frac{\partial}{\partial z} [\frac{\partial^2\psi_2^*}{\partial z \partial \bar{z}}]d\bar{z} - \frac{\partial}{\partial \bar{z}} [\frac{\partial^2\psi_2^*}{\partial z \partial \bar{z}}]dz \right\}$$

or

$$P = -96\pi D(1 - r_0^2)(2 - 3r_0^2)\varepsilon^2 r_0^2 \cos 2\theta_0 \tag{A4.2}$$

Thus from Eq. (A4.2), it is seen that the force expression has a zero at $r_0^2 = \frac{2}{3}$, which is incompatible with the real situation.

Now using $\psi_1^*(z,w)$ instead of $\psi_2^*(z,w)$ in Eq. (A4.1a), the expression for P with $\theta_0 = 0$ is

$$P = 24\pi D\varepsilon^2 r_0^2(1 - r_0^2) \qquad \text{(A4.3; 1.79)}$$

Equation (A4.3) does not have a zero for

$$0 < r_0 < 1.$$

APPENDIX 5

Reduced Equations for Plates

a) Plate Nos. 1 and 4

Substituting Eq. (1.34) in Eq. (1.33), we get

$$
\begin{aligned}
&{}_p\rho_i\{\ddot{\chi}_{i,1} + J_0(\lambda_0,r)\ddot{a}_{i,13} + (r-1)r^2\,\ddot{a}_{i,14} + (r-1)r^3\,\ddot{a}_{i,15} \\
&+ [J_1(\lambda_1 r)\ddot{a}_{1,7} + (r-1)r\,\ddot{a}_{i,8} + (r-1)r^2\,\ddot{a}_{i,9}]\cos\theta + [J_1(\lambda_1 r)\ddot{a}_{i,10} \\
&+ (r-1)r\,\ddot{a}_{i,11} + (r-1)r^2\,\ddot{a}_{i,12}]\sin\theta + [J_2(\lambda_2 r)\ddot{a}_{i,1} + (r-1)r^2\,\ddot{a}_{i,2} \\
&+ (r-1)r^3\,\ddot{a}_{i,3}]\cos 2\theta + [J_2(\lambda_2 r)\ddot{a}_{i,4} + (r-1)r^2\,\ddot{a}_{i,5} \\
&+ (r-1)r^3\,\ddot{a}_{i,6}]\sin 2\theta + (r^2\log r)\ddot{\chi}_{i,7} + \psi_{i,8}\ddot{\chi}_{i,8} + \psi_{i,9}\ddot{\chi}_{i,9} \\
&+ \psi_{i,10}\ddot{\chi}_{i,10} + \psi_{i,11}\ddot{\chi}_{i,11}\} + ({}_pD_i)\frac{1}{a_B^3}(1 + {}_p\mu_i)({}_p\kappa_{i,0})\sin {}_p\beta_i(\sin\theta \\
&+ \cos\theta)(\frac{d}{dt} - 1)\{\lambda_0^3 J_1(\lambda_0 r)a_{i,13} + 9a_{i,14} + (32r - 9)a_{i,5} \\
&+ [\frac{\lambda_1^2}{r} J_1(\lambda_1 r)\sin\theta + \lambda_1^2(\frac{1}{r} J_1(\lambda_1 r) - \lambda_1 J_0(\lambda_1 r))\cos\theta]a_{i,7} - \frac{3}{r}\sin\theta\, a_{i,8} \\
&+ [(\frac{3}{r} - 8)\sin\theta + 8\cos\theta]a_{i,9} + [-\frac{\lambda_1^2}{r} J_1(\lambda_1 r)\cos\theta + \lambda_1^2(\frac{1}{r} J_1(\lambda_1 r) \\
&- \lambda_1 J_0(\lambda_1 r))\sin\theta]a_{i,10} + \frac{3}{r}\cos\theta\, a_{i,11} + [8\sin\theta - (\frac{3}{r} - 8)\cos\theta]a_{i,12} \\
&+ [\frac{2\lambda_2^2}{r} J_2(\lambda_2 r)\sin 2\theta + (\frac{2\lambda_2^2}{r} J_2(\lambda_2 r) - \lambda_2^3 J_1(\lambda_1 r))\cos 2\theta]a_{i,1} \\
&+ 5(\cos 2\theta - 2\sin 2\theta)a_{i,2} + [(24r-5)\cos 2\theta - (24r-10)\sin 2\theta]a_{i,3} \\
&+ [-\frac{2\lambda_2^2}{r} J_2(\lambda_2 r)\cos 2\theta + (\frac{2\lambda_2^2}{r} J_2(\lambda_2 r) - \lambda_2^3 J_1(\lambda_1 r))\sin 2\theta]a_{i,4}
\end{aligned}
$$

$$+ 5(\sin 2\theta + 2\cos 2\theta)a_{i,5} + [(24r-5)\sin 2\theta + (24r-10)\cos 2\theta]a_{i,6}$$

$$+ \frac{4}{r}\chi_{i,7} + \sum_{j=8}^{11}\chi_{i,j}\frac{8}{r}[r^2 - 2rr_j\cos(\theta-\theta_j) + r_j^2]^{-1}[1 - 2rr_j\cos(\theta-\theta_j)$$

$$+ r^2r_j^2]^{-2}(1-r_j^2)\{r^2(1+2r_j^2) - rr_j[\cos(\theta-\theta_j) + \sin(\theta-\theta_j)]$$

$$- r^3r_j(2+r_j^2)[\cos(\theta-\theta_j) - \sin(\theta-\theta_j)] + r^4r_j^2[\cos 2(\theta-\theta_j) + \sin 2(\theta-\theta_j)]\}\}$$

$$- {}_p\rho_i(\omega_{B,1}^2 + \omega_{B,2}^2)\chi_i - \frac{1}{a_B^4}({}_pD_i)\{\lambda_0^4J_0(\lambda_0r)a_{i,13} + \frac{9}{r}a_{i,14} + (64 - \frac{9}{r})a_{i,15}$$

$$+ \lambda_1^4J_1(\lambda_1r)\cos\theta\, a_{i,7} - \frac{3}{r^2}\cos\theta\, a_{i,8} + \frac{3}{r^2}\cos\theta\, a_{i,9} + \lambda_1^4J_1(\lambda_1r)\sin\theta\, a_{i,10}$$

$$- \frac{3}{r^2}\sin\theta\, a_{i,11} + \frac{3}{r^2}\sin\theta\, a_{i,12} + \lambda_2^4J_2(\lambda_2r)\cos 2\theta\, a_{i,1} - \frac{15}{r}\cos 2\theta\, a_{i,2}$$

$$+ \frac{15}{r}\cos 2\theta\, a_{i,3} + \lambda_2^4J_2(\lambda_2r)\sin 2\theta\, a_{i,4} - \frac{15}{r}\sin 2\theta\, a_{i,5} + \frac{15}{r}\sin 2\theta\, a_{i,6}\}$$

$$= (\omega_{B,1}^2 + \omega_{B,2}^2)R_i + (\dot{\omega}_{B,2} - \omega_{B,1}\omega_{B,3})a_Br\cos\theta$$

$$- (\dot{\omega}_{B,1} + \omega_{B,2}\omega_{B,3})a_Br\sin\theta - {}_p\rho_i[\mathscr{I}_3]\{G_B\underline{\ddot{q}}_B^* + [2\omega_B$$

$$+ \frac{1}{\|M\|_B}(\frac{1}{\gamma}\tau_1 - \tau_2)]G_B\underline{\dot{q}}_B^* + [\tilde{\dot{\omega}}_B + \tilde{\omega}_B\tilde{\omega}_B + \frac{1}{\|M\|_B}(\frac{1}{\gamma}\tau_1 - \tau_2)]G_B\underline{q}_B^*$$

$$- \frac{1}{\|M\|_B}(\tau_9\dot{\theta}^* + \tau_3\theta^*)\} \qquad \text{(A5.1)}$$

b) Plate Nos. 2 and 3

Equations for the plates Nos.2 and 3 are similar to the above equation. The only difference is that these will involve twelve more functions of the form $\psi_i(z,w)$ introduced in Eq. (1.38).